

Article

Influence of the Nitrogen Precursor in the Development of N-Functionalities in a Mesoporous Carbon Material and Its Effect on the Li–S Cells’ Electrochemistry

Carolina Mejía Salazar ¹, Julián Acevedo ¹, Jennifer Laverde ² and Diana López ^{1,*}

¹ Química de Recursos Energéticos y Medio Ambiente, Instituto de Química, Facultad de Ciencias Exactas y Naturales, Universidad de Antioquia, Calle 70 No. 52-21, Medellín 050010, Colombia; carolina.mejia4@udea.edu.co (C.M.S.); julian.acevedom@udea.edu.co (J.A.)

² Grupo de Materiales Avanzados y Energía MATyER, Facultad de Ingeniería, Instituto Tecnológico Metropolitano-ITM, Carrera 31 # 54-10, Medellín 050013, Colombia; jenniferlaverde@itm.edu.co

* Correspondence: diana.lopez@udea.edu.co

Abstract: Li–S batteries are positioned as a strong alternative for efficient energy storage due to their high theoretical energy density and their theoretical specific capacity (1675 mA h g^{-1}) compared to current Li-ion batteries; however, their commercialization is affected by the rapid decay of the specific capacity as a consequence of the different species of lithium polysulfides that are generated during the charge–discharge processes. The use of nitrogen-doped mesoporous carbon materials has been shown to have the ability to confer electronic conductivity to sulfur and retain the lithium polysulfide species. However, there are not enough studies to help understand how the type of nitrogen precursor influences the development of specific nitrogen functionalities to favor the retention of lithium polysulfide species. This work seeks to determine the effect of the use of different nitrogen precursors on the structural changes of the mesoporous carbon materials prepared, and thus evaluate the electrochemical behavior of Li–S cells correlating the type of nitrogen functionality generated when the precursor is varied with the charge/discharge capacity developed during the cell operation. For this study, different carbon materials were prepared by the variation of the nitrogen source (melamine, ethylenediamine, and hexadecylamine) to obtain a N-doped mesoporous carbon with different distributions of nitrogen functionalities in its structure. The use of the primary amine ethylenediamine as a nitrogen precursor in the formation of structured carbon materials favored elemental sulfur infiltration into its pores, resulting in the maximum sulfur content within the pores and interacting with the carbonaceous matrix (78.8 wt.%). The carbon material prepared with this precursor resulted in a higher content of N-pyridinic functionality, which, combined with the high content of N-pyrrolic, resulted in the highest specific discharge capacity at 0.1 C after 100 cycles when compared to cells assembled with materials derived from the use of melamine and hexadecylamine precursors. The cell assembled with the electrode formed from ethylenediamine as a nitrogen precursor presented an initial discharge capacity of 918 mA h g^{-1} with a Coulombic efficiency of ~83.4% at 0.1 C after 100 cycles.

Keywords: mesoporous carbon; nitrogen functionalities; Li–S batteries; lithium polysulfide anchoring; electrochemical behavior



Citation: Mejía Salazar, C.; Acevedo, J.; Laverde, J.; López, D. Influence of the Nitrogen Precursor in the Development of N-Functionalities in a Mesoporous Carbon Material and Its Effect on the Li–S Cells’ Electrochemistry. *Batteries* **2024**, *10*, 169. <https://doi.org/10.3390/batteries10060169>

Academic Editor: Torsten Brezesinski

Received: 2 May 2024

Revised: 17 May 2024

Accepted: 20 May 2024

Published: 21 May 2024



Copyright: © 2024 by the authors. Licensee MDPI, Basel, Switzerland. This article is an open access article distributed under the terms and conditions of the Creative Commons Attribution (CC BY) license (<https://creativecommons.org/licenses/by/4.0/>).

1. Introduction

The growth of today’s society towards a digitalized and electrified future implies an increase in energy demand, posing several major challenges for today’s energy industry. This high level of energy consumption calls for the development of more efficient and sustainable systems. Batteries are electrochemical devices that store electrical energy in the form of chemical energy; the development of high-energy-density storage devices is of great interest. Lithium-ion batteries offer better performance than conventional nickel

systems because they possess a higher specific energy of around 250–300 W h kg⁻¹ [1] than the 50–75 W h kg⁻¹ of NiCd batteries [2], allowing them to store a considerable amount of energy in a relatively small mass; this has been essential for the development of electric vehicles and mobile devices [3]. However, the main challenge for these conventional Li-ion batteries is the dependence on expensive and scarce materials for their large-scale production and the safety concerns, hence, there is a need to use more environmentally friendly materials [4].

Lithium–sulfur (Li–S) batteries are a promising alternative because of their high theoretical specific capacity of 1675 mA h g⁻¹ and a theoretical energy density of 2500 W h kg⁻¹ [5] and because sulfur is a material very abundant in nature, low-cost, non-toxic and offers good safety due to its protection from being overcharged [6]. Li–S battery systems work by the reduction of elemental sulfur and the oxidation of the metallic lithium through the discharge process, to obtain lithium polysulfides (LiPSs), that are responsible for the loss of capacity of these systems, at the end Li₂S is generated, and is related to the volumetric change in the cathode due to its lower density compared to sulfur, producing, among other things, cracking of the materials, loss of active material and lower contact at the interface [7]. Furthermore, LiPSs are highly soluble in the liquid electrolytes typically used, resulting in reduced ionic mobility and possible anode corrosion, leading to rapid capacity degradation [8].

One approach to overcome these challenges and bring Li–S batteries closer to the market was performed by Shi et al. [9], who developed a gel polymer electrolyte as a catholyte to stabilize the sulfurized polyacrylonitrile used as an active material. Additionally, the technique most commonly used follows the lines of the work carried out by Nazar et al. [10] where the mesoporous carbon material CMK-3 was proposed as a sulfur host because of the conductive and sorption properties of the carbon framework. In addition to electrical properties, carbon substrates have also been studied because of their mechanical properties that make them adequate materials to produce flexible batteries [11].

Despite the good properties of carbon materials, they can be enhanced by the inclusion of heteroatoms, like nitrogen. Especially, the nitrogen functionalities can help anchor the LiPSs, leading to greater specific capacity and lower capacity loss [12,13]. For a nitrogen-enriched mesoporous carbon, Sun et al. [14] demonstrated that nitrogen doping in the right concentration range (4–8 wt.%) could improve the carbon electrical conductivity and provide faster charge-transfer kinetics. In addition to the retention of LiPSs, Qiu et al. [15] reported that nitrogen doping facilitates the disproportionation of polysulfide anions; however, these nitrogen species do not strictly act as catalysts but shift the chemical equilibrium, favoring the oxidation of LiPSs to form elemental sulfur. Likewise, numerous computational and theoretical studies have identified the effect of the different nitrogen functionalities; pyridine and pyrrolic nitrogen favors the anchoring and retention of polysulfide species [16,17] mainly due to the bonding between nitrogen and lithium; however, it is preferable to have a greater portion of pyridinic nitrogen because it serves as an active center to reduce the activation barrier for the Li₂S decomposition [18]. Therefore, graphitic (or quaternary) nitrogen may also be present, which is embedded in the plane of the carbon network and has a high electronegativity that favors charge transfer processes [14,19–21]. The three nitrogen functionalities commonly coexist in the prepared materials, making it difficult to favor one over the others to increase any of the properties associated with a specific functionality.

Recognizing the effect that each nitrogen functionality can have on electrochemical performance, this work aims to evaluate the effect of different nitrogen precursors on the favoring of the nitrogen functionalities, the physicochemical properties of the CMK-3-type material, and how these properties can be related to the electrochemical behavior of the assembled cell. Hence, nitrogen-doped mesoporous carbon materials were prepared using the mesoporous silica template SBA-15 to obtain a CMK-3-type material with nitrogen functionalities in its structure. To perform the N-doping, three different nitrogen sources were used: hexadecylamine, melamine, and ethylenediamine.

2. Materials and Methods

2.1. Nitrogen-Doped Mesoporous Carbon Preparation

For the preparation of the mesoporous carbon materials, the methodology proposed by Hang T.T. Le et al. was employed [22]. The carbon materials were obtained by using mesoporous silica SBA-15 as a template. During the initial preparation step, 1.0 g of SBA-15 was mixed with 10 mL of sucrose 0.4 M and 0.08 mL of H₂SO₄ (95–97 v/v.% Merck). To ensure that the sucrose solution was evenly distributed within the silica pores, the sucrose solution was subjected to an hour of ultrasonic treatment followed by heat treatment at 100 °C for 6 h, and then, the temperature was increased to 160 °C for 6 h. The second step involved adding nitrogen to obtain N-doped mesoporous carbon materials. To change the type of nitrogen functionality that forms during the carbonization process, three nitrogen sources were chosen, including two short and long-linear chain primary amines (ethylenediamine and hexadecylamine, respectively), and a cyclic amine (melamine). The material formed in step 1 and the nitrogen precursor were mixed using a mass ratio of 5:1. Then, it was thermally activated at 100 °C for 6 h followed by a carbonization process in an inert environment (N₂) at 850 °C for 3 h. This carbonization temperature was selected to obtain a graphitic structure that is favored at high temperatures, improving the formation of the number of 6-membered rings [23].

The silica template was eliminated by soaking the carbon material in a 10 v/v.% HF solution for 12 h. Finally, the resulting material was neutralized and dried at 100 °C for 12 h. According to the nitrogen sources used, the materials were labeled as MCE, MCM, and MCH (ethylenediamine, melamine, and hexadecylamine, respectively).

2.2. Sulfur Incorporation in the Mesoporous Carbon Materials

To obtain S/C materials to be used in the cathode formation, the melt infiltration strategy was employed according to the experimental parameters found in a previous work. The S/C materials were obtained according to previous studies related to the S/C ratio where it was found that the best proportion was 90/10 [22]. The sulfur infiltrated materials were formed by mixing the carbon material with elemental sulfur for 15 min, using a ratio of 90:10 respectively. A solution of CS₂ (99.5 v/v% PanReac) was added to the previous mixture to obtain a homogeneous distribution of sulfur on the carbon material surface. For this, the suspension was stirred for 30 min and the solvent was subsequently evaporated. The mixture of carbon material and sulfur was heat treated at 155 °C for 6 h in a stainless-steel autoclave to melt the sulfur and incorporate it into the pores of the carbon material. The samples were labeled as MCE-S, MCM-S, and MCH-S indicating the sulfur incorporation to form the S/C materials.

2.3. Physicochemical Characterization

To determine the nitrogen functionalities formed in the carbon material using the different nitrogen precursors and correlate them with the electrochemical behavior of a Li–S battery, several characterization techniques were used to evaluate the structure of the material, composition, morphology, and amount of sulfur found on the surface and in the pores of the S/C materials. Thermogravimetric analysis (TGA-DTG, SDT-Q600 TA Instruments) was carried out to evaluate the thermal stability of the carbon materials and to know the infiltrated sulfur content and its interaction with the carbon structure. For this purpose, a nitrogen atmosphere was employed, and a heating rate of 5 °C/min from room temperature up to 600 °C with a nitrogen flow of 100 mL min⁻¹. The determination of the textural properties of the materials before and after sulfur infiltration was carried out using the nitrogen adsorption/desorption technique at 77 K (ASAP 2020) through the Brunauer–Emmet–Teller (BET) approximation to determine the surface, pore volume, and pore size distribution. X-ray diffraction was used to determine the incorporation of sulfur within the pores of the carbon material by monitoring the diffraction peaks of elemental sulfur. A Malvern-PANalytical diffractometer model Empyrean 2012, with Pixel 3D detector and Cu K radiation was used from 5° up to 90° in 0.01° steps. The sulfur distribution in the

S/C materials was studied with the use of scanning electron microscopy (FE-SEM JEOL JSM-7100F system coupled with an Oxford energy dispersive spectroscopy, EDX). Raman spectroscopy was carried out to determine the changes in the graphitization degree of the materials when nitrogen was incorporated into the carbon structure using a Horiba Jobin Yvon, Labram HR instrument with a wavelength of 632.8 nm. The signals were normalized concerning the D band intensity. The Raman spectra were mathematically decomposed into 4 bands, these were normalized and averaged to perform the deconvolution of the spectra using Voigt curves with the support of CasaXPS Version 2.3.23PR1.0 software. Finally, to determine the changes generated in the nitrogen functionalities due to the use of different precursors, elemental analysis (LECO Truspec CHNS-O) was carried out and focused on the nitrogen content in the bulk of the materials. The nitrogen and sulfur functionalities and their content in the material surface were elucidated from X-ray photoelectron spectroscopy (XPS, Specs X NAP-XPS with PHOIBOS 150 1D-DLD as analyzer). The CASA XPS program was used to quantify the elemental composition using a Gaussian-Lorentzian mix function with Shirley background subtraction.

2.4. Electrochemical Characterization

To evaluate the electrochemical behavior of the different S/C materials in Li–S batteries, coin-type cells (CR2032) were assembled. For this purpose, 70 mg of the sulfur infiltrated materials, 15 mg of PVDF (Aldrich, St. Louis, MO, USA), and 15 mg of Acetylene Black were dispersed in 700 μL of N-methyl pyrrolidone (NMP, Merck, Darmstadt, Germany) for 12 h; the mixture was dispersed on an aluminum foil using the Doctor Blade technique maintaining a thickness of 350 μm and it was dried at 60 $^{\circ}\text{C}$ to avoid sulfur sublimation. Electrodes of 1.2 cm diameter were cut with a sulfur loading of 0.30, 0.31, and 0.20 mg/cm^2 for MCE, MCM, and MCH respectively. The electrolyte was prepared by dissolving the salt lithium bis-(trifluoromethanesulphonyl) imide (1M) (LiTFSI, 99.95 wt.% Aldrich, St. Louis, MO, USA) and LiNO₃ (0.1 M) (99.99 wt.%, Sigma-Aldrich, St. Louis, MO, USA) in a 1:1 *v/v* solution of dimethoxymethane (DME, $\geq 99\text{ v/v\%}$ Aldrich) and 1,3-dioxolane (DOL, 99.5 *v/v\%* Aldrich). The Li–S cells were assembled using the S/C materials as a working electrode, metallic lithium as a counter electrode (0.75 mm thick \times 19 mm wide, Aldrich), and porous propylene as a separator (Celgard 2500, MTI Corp., Berkeley, USA) with 600 μL of electrolyte; a controlled atmosphere was used in an Ar-filled glove box ($[\text{H}_2\text{O}]$ and $[\text{O}_2] < 0.5\text{ ppm}$). For the electrochemical tests, a Battery Test Equipment LBT 21084 (Arbin Instruments) was used variating the C-rate from 0.1 to 10 C between 1.7 and 2.8 V vs. Li/Li⁺. The cell was operated in constant current (CC) mode at room temperature. Electrochemical impedance (EIS) was performed with an amplitude of 10 mV in the frequency range of 1 MHz to 10 mHz. Cyclic voltammetry (CV) was carried out in a potential window of 1.7–2.8 V vs. Li/Li⁺ at a scan rate of 0.1 mV s⁻¹.

3. Results

3.1. Physicochemical Characterization of the Carbon Materials and the Corresponding S/C Materials

Effect of Nitrogen Precursor on the Physicochemical Properties

Figure 1A depicts the thermogravimetric (TGA-DTG) analysis of the nitrogen-modified carbon materials before sulfur infiltration. A first thermal event related to moisture loss can be observed for the three materials at temperatures below 150 $^{\circ}\text{C}$. There is no evidence of significant mass losses between 200 $^{\circ}\text{C}$ and 500 $^{\circ}\text{C}$, showing that the carbon materials are stable; nevertheless, a weight loss can be observed above 500 $^{\circ}\text{C}$, indicating that the material was not completely carbonized [24]. Due to the structural differences between the nitrogen precursors, carbon materials generated from ethylenediamine and hexadecylamine are projected to favor aliphatic structures over those formed from melamine, whose structure is cyclic. During the polymerization of carbon, the amino groups that are present in the melamine structure favored the formation of graphitic compounds. The global weight losses for the materials were 34.5, 31.9, and 37.3 wt.% for MCE, MCM, and MCH respectively.

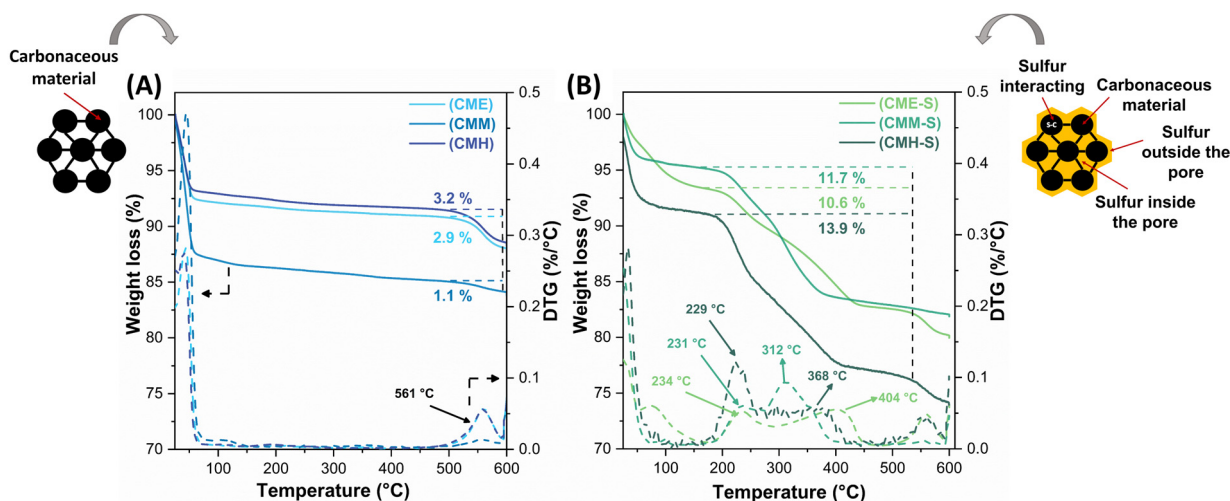


Figure 1. Thermal (DTG) behavior of the carbon materials (A) before and (B) after sulfur infiltration.

Figure 1B presents the thermal stability (TGA-DTG) results for the formed S/C materials. The materials exhibit mass loss in the temperature range of 150–450 °C; given that carbon materials without sulfur infiltration (Figure 1A) do not exhibit mass loss in this temperature range, the mass losses can be attributed to the sublimation of elemental sulfur present in the S/C materials. Weight losses of 10.6, 11.7, and 13.9 wt.% are observed for the samples MCE-S, MCM-S, and MCH-S respectively varying the temperatures at which each of them loses elemental sulfur. Although the nominal amount of sulfur in the samples was 10 wt.%, the MCM-S and MCH-S materials exhibited a low sulfur confinement in the S/C materials. This could be because, during the sulfur infiltration process, CS₂ is used as a solvent, and according to some studies can promote the formation of C-S bonds in the carbon structure [25]. C-S bonds have a similar binding energy to S-S bonds [26], so the breakage of C-S bonds during heat treatment in an inert atmosphere to determine total sulfur content may contribute to the overall loss of sulfur measured by the thermal analyzer.

Sulfur sublimation temperatures reflect the strength with which it interacts with the carbon matrix, which helps to determine which of the carbon materials was able to infiltrate sulfur more efficiently. Carbon materials with more sulfur incorporation within the pores or interacting with the carbon matrix are expected to have better electrochemical performance than those with sulfur outside the porous structure [27]. Elemental sulfur sublimes in a single step, resulting in a single peak in the DTG analysis; however, as shown in Figure 1B, sulfur sublimes in multiple steps, revealing various sulfur environments in the S/C materials. According to Suzuki et al., there are three types of chemical environments for sulfur: sulfur outside the pore sublimes below 280 °C, while sulfur inside the pores between 280 and 400 °C and sulfur interacting with the carbon matrix at temperatures > 400 °C [28]. Accordingly, the sulfur content outside the pores for the samples MCE-S, MCM-S, and MCH-S was 23.2 wt.%, 28.6 wt.%, and 39.5 wt.%, respectively, implying that the electrochemical performance through the cycles of MCH-S should be the lowest due to the possibility of sulfur lixiviation into the electrolyte and the possible loss of electronic conductivity caused by sulfur's non-optimal interaction with the carbonaceous matrix. On the other hand, MCE-E has the highest amount of sulfur available for oxide-reduction processes (76.8 wt.%) followed by MCM-S (71.4 wt.%) and MCH-S (60.5 wt%) (Figure S1).

Figure 2A,B displays the adsorption–desorption isotherms of N₂ at 77 K for each sample. According to IUPAC nomenclature, all samples possess a type IV isotherm [29]. First, the isotherm shape did not change after the inclusion of sulfur in the samples, indicating that the porous system has remained the same, not collapsed, or not completely clogged. The presence of a hysteresis loop is characteristic of mesoporous materials, and the pore size distribution shows primary pores around 4 nm [30].

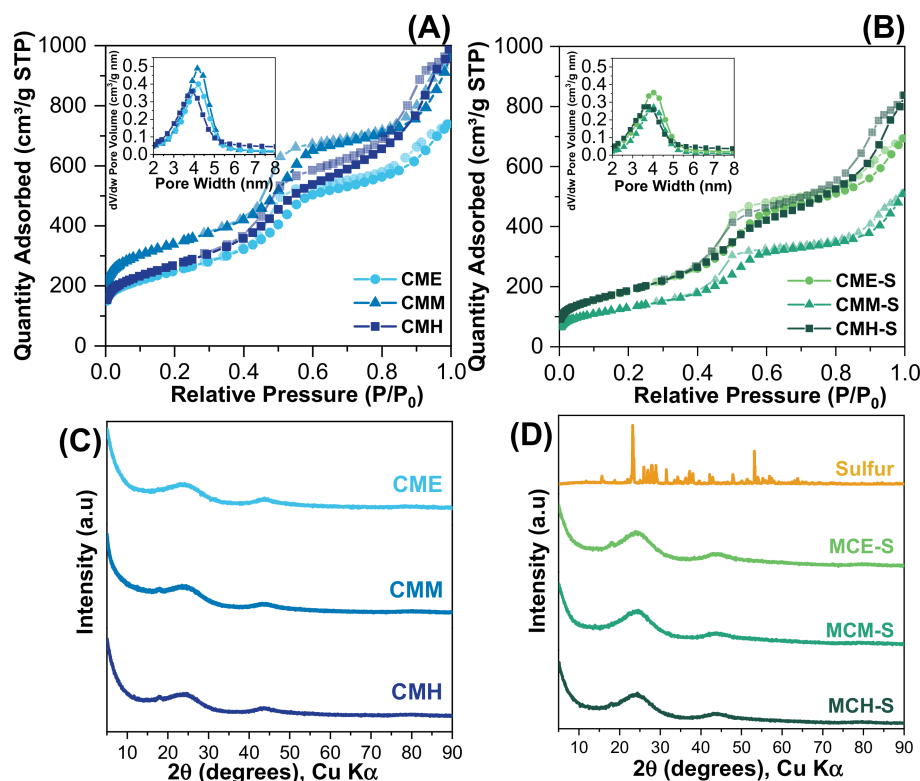


Figure 2. N₂ adsorption–desorption isotherms for (A) mesoporous carbons and (B) mesoporous carbons with sulfur. XRD patterns of the (C) carbon materials and (D) S/C materials.

Textural properties are listed in Table 1; as expected, there is a diminishing of specific surface area, pore volume, and pore diameter due to sulfur infiltration and channel narrowing. The thermal decomposition of melamine results in the release of NH₃ and N₂ [31,32], and the high nitrogen content of this precursor could result in a greater release of gases compared with hexadecylamine and ethylenediamine, causing pore development and higher surface area.

Table 1. Textural properties of mesoporous carbons and A_{D1}/A_G band ratio.

Sample	S _{BET} (m ² /g)	V _T (cm ³ /g)	D _p (nm)	A _{D1} /A _G
MCE	885	1.2	4.2	3.9
MCM	1219	1.5	4.2	4.4
MCH	956	1.5	3.9	4.1
MCE-S	676	1.1	4.0	4.2
MCM-S	462	0.78	4.0	4.3
MCH-S	681	1.3	3.7	5.7

The XRD patterns for the carbon materials before and after sulfur incorporation are presented in Figure 2C,D; elemental sulfur is included as a reference pattern. The XRD patterns for MCE, MCM, and MCH are comparatively displayed in Figure 2C; the two distinct reflection peaks of its amorphous graphitic structure are seen at $2\theta = 25^\circ$ and 45° , corresponding to the (002) and (011) planes respectively (ICSD 98-061-7290), which indicate the presence of the hexagonal ordered structure for CMK-3 carbon materials type [33]. Figure 2D shows the diffraction pattern for elemental sulfur, the observed peaks correspond to the orthorhombic sulfur phase. The CMH and CMM materials present a diffraction peak close to 20° that is related to the (101) plane due to the introduction of heteroatoms in the structure [34].

According to what was reported, it is expected that no signals related to elemental sulfur diffraction peaks will be observed when the sulfur infiltrated material is formed, as this would imply a high dispersion of sulfur in the pores of the materials or the formation of a very thin layer with a small crystallite size [35,36]. The absence of sulfur-related peaks in the three samples studied indicates that sulfur was efficiently integrated into the carbon material achieving a homogenous sulfur dispersion; this characteristic is required for optimum electrochemical performance.

To know the morphology of the prepared materials and the sulfur distribution after the formation of the S/C materials, scanning electron microscopy (SEM) was used, and SEM-EDS allows mapping of the elements present in the materials; this technique helps to determine the successful replication of the template, if morphological modifications were made after the sulfur incorporation, and if the distribution of sulfur was uniform. Figure 3 shows the micrographs for each material, and rod-like structures corresponding to the replication of the SBA-15 silica template are observed [37,38]. From the elemental mapping, it can be observed that sulfur is uniformly distributed over the entire surface as there are no sulfur agglomeration points in specific regions.

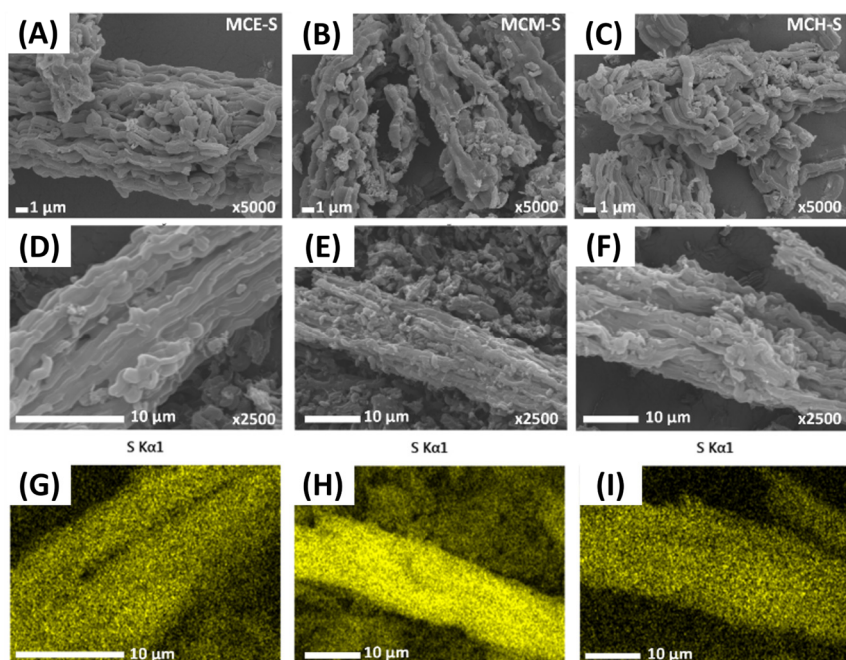


Figure 3. SEM images for MCE-S (A,D), MCM-S (B,E), and MCH-S (C,F), and sulfur mapping for MCE-S, MCM-S, and MCH-S respectively (G–I).

Raman spectroscopy was used to study the degree of graphitization of the prepared mesoporous carbons. This technique permits identifying the structural changes inherent to the carbon network due to the precursor used and correlating them with the conductive and electron transfer properties. The data obtained were treated the same way for each sample; the spectra have the same scale and are normalized by the peak of highest intensity, and a mathematical deconvolution into four main peaks was performed, as shown in Figure S2. The two principal bands are D_1 and G , located at $\sim 1325\text{ cm}^{-1}$ and $\sim 1590\text{ cm}^{-1}$, respectively [39]. D_1 band is mainly attributed to the disorder, i.e., the presence of tetrahedral carbon atoms and heteroatoms disrupting the hexagonal sp^2 network, and G is associated with the stretching mode of sp^2 carbons that compose the graphitic plane [40]. The other two bands located at $\sim 1150\text{ cm}^{-1}$ (D_4) and $\sim 1530\text{ cm}^{-1}$ (D_3) are also related to the disorder [41]. D_3 is related to interstitial defects of amorphous sp^2 species, including functionalized small molecules [42], and D_4 to aliphatic portions and defects of the network border [39,43]. The ratio between the integrated area of bands D_1 and G (A_{D_1}/A_G) gives

insight into the graphitization degree; as shown in Table 1, MCH, MCM, and MCE have A_{D1}/A_G of 4.1, 4.4, and 3.9, respectively, indicating that melamine-based mesoporous carbon has a relative more disordered structure, due to the higher content of nitrogen that causes defects in the material structure affecting the sp^2 hybridized carbon. The presence of nitrogen in the quaternary form impedes electronic conductivity within layers affecting the graphitization properties [44,45]. Higher graphitic samples have a non-polar surface, which could lead to better sulfur infiltration through the mesoporous system [46]. This agrees with the previous results for MCM-S. It possesses the highest amount of nitrogen, lowering the graphitization degree, preventing effective sulfur infiltration through the pores, and causing pore blocking, lower pore volumes, and sulfur losses below 400 °C. For the infiltrated samples, it is observed that the values for A_{D1}/A_G are almost the same as for the corresponding samples without sulfur, except for MCH-S, for this sample the primary carbon structure could be altered by the sulfur infiltration process lowering graphitization.

The electrochemical performance of batteries depends significantly on the different functionalities developed in the carbon materials. In this work, by varying the nitrogen source in the preparation of mesoporous carbons, it is expected that the nitrogen functionalities will show a differentiation, helping to understand the conditions necessary to favor the desired type of functionality. To determine the effect of the precursor on the nitrogen functionality developed in the carbon materials, elemental analysis was carried out to determine the content of nitrogen, carbon, and oxygen. Table 2 shows the elemental content of the carbon materials prepared using two techniques: elemental analysis, which represents the composition in the bulk of the materials, and XPS, which reflects the composition at the materials' surface. The carbon content in the bulk of the materials evidences the effect of the precursors used according to their chemical structure, which affects the organization of the atoms in the carbon material. The material formed from the precursor melamine has the lowest and highest carbon (75 wt.%) and nitrogen (3.8 wt.%) content, respectively. This is because the chemical structure of melamine is primarily a six-member ring with three nitrogen atoms at its vertices, as well as -NH₂ groups, which favors the formation of a mainly nitrogenous carbon structure during the polymerization phase. The above is reflected in the C/N ratio, with the MCM-S material having the lowest value. Carbon materials with comparable carbon and nitrogen content were formed using ethylenediamine and hexadecylamine as nitrogen precursors; however, the C/N ratio was higher for the MCE-S. These two precursors are primary amines, which are very reactive and so promote polymerization. Since ethylenediamine includes two terminal amino groups, there are two polymerization locations for carbon formation, leaving nitrogen to create the final chemical structure, resulting in a lower C/N ratio than that achieved with the hexadecylamine precursor. The oxygen content seen in Table 2 is due to the use of sucrose in the preparation of the carbon materials. A high weight percentage can have a substantial impact on the performance of Li–S batteries because it promotes the breakdown of lithium polysulfides in the electrolyte, increasing its viscosity and favoring the deposition of solid species on the anode [47]. The lowest C/O ratio is obtained for the MCM-S material (10) indicating a higher proportion of oxygenated functionalities in the carbon structure obtained. On the other hand, the MCH-S material presents the highest C/O ratio; however, the electrochemical performance of the Li–S batteries depend on parameters such as elemental content and degree of graphitization that provide the electron conductive characteristics.

Table 2. Elemental composition of the S/C materials quantified by elemental analysis and XPS.

Sample	XPS (wt.%)						Elemental Analysis (wt.%)			
	C	N	O	H	C/N	C/O	C	N	O	S
MCE-S	84	1.7	3.2	1.0	49	26	90	0.8	6.0	3.2
MCM-S	75	3.8	7.5	1.8	20	10	89	1.8	5.8	3.9
MCH-S	81	1.8	2.1	0.8	45	37	89	0.4	7.4	3.0

Electrochemical reactions occur mainly on the surface; hence it is essential to know the elemental composition and the type of surface functionalities of the materials. In the study obtained by XPS, four peaks were detected as C1s (284.5 eV), N1s (~400 eV), O1s (~532.5 eV), and S2p (~169.5 eV). Table 2 shows the total elemental composition at the surface of the materials. The carbon content of the three materials is comparable at the surface, but the nitrogen and oxygen content vary depending on the precursor used. Melamine is the precursor with the highest surface nitrogen content, whereas hexadecylamine has the lowest. The above is related to the chemical structure of each precursor, with melamine having the highest nitrogen content.

An important factor in the development of carbon materials to be used as cathodes for Li–S batteries is the type of functionality that is developed. In the case of nitrogen, a higher content of pyridine-type functionality is preferred to trap lithium polysulfide species, although there is also a contribution from the pyrrolic-type functionality. As for quaternary-type nitrogen, this is mainly related to the possibility of retaining electron conduction properties through the carbon structure [48]. The HR-XPS spectra for sulfur (S2p) and nitrogen (N1s), along with the percentage of each type of functionality produced in carbon materials, are displayed in Figure 4. The deconvoluted spectra for nitrogen N1s for the carbon materials after sulfur incorporation is presented in Figure 4A; here, the samples show four main peaks related to N-pyridinic (~396–398 eV), N-pyrrolic (~399–400 eV), N-quaternary and the oxidized form (>400 eV). Depending on the precursor used, the signals tend to shift which is typically associated with the existence or absence of chemical states of the element that have distinct formal oxidation states [49]. When heteroatoms with higher electronegativity than nitrogen are present, the electron density decreases, and the nitrogen signal shifts towards more positive values. The substantial oxygen content in each sample will influence where the nitrogen peaks are located. Both N-pyridinic and N-pyrrolic functionalities are required for superior electrochemical behavior; the former is most closely linked to the retention of lithium polysulfide species. From Figure 4B, while there was a higher N-pyrrolic content in all three materials, MCE-S showed the highest percentage of pyridine functionality, followed by MCM-S and MCE-S. The MCE-S material comprises 53.3 at.% due to the combined contribution of both functionalities, which increases the likelihood of retaining lithium polysulfide species generated during redox processes and the possibility of reducing the shuttle effect problems.

The MCM-S material has the highest content of N-quaternary type (~44.2 at.%), followed by MCE-S (~33.1 at.%), and MCH-S (~26 at.%). Nevertheless, obtaining proper functionalization with N-pyridinic and N-pyrrolic is crucial to prevent polysulfide species from dissolving in the electrolyte and deactivating the batteries. This is in addition to the importance of the materials' electronic conductivity. On the other hand, MCH-S presents the highest N-oxidized functionality decreasing the likelihood of trapping lithium polysulfide species, which will be reflected in the battery's specific capacity.

Computational studies support the idea of improving the capacity of Li–S batteries when nitrogen functionalities are introduced; it has been found that the retention of lithium polysulfides is favored by the presence of pyridine and pyrrolic nitrogen since, through their free electronic pairs, strong interaction with Li^+ is generated, causing the discharge capacity to be maintained through the cycles. The relationship between the inclusion of nitrogen in the carbonaceous structure with the electrochemical performance was demonstrated, where the cells that are formed of S/C materials without nitrogen doping showed lower discharge capacity [50,51].

Figure 4C shows the XPS results of sulfur for the samples after sulfur incorporation. The total sulfur content in the surface for MCE-S, MCM-S, and MCH-S was 3.2 at.%, 3.9 at.%, and 3.0 at.%, respectively. Three peaks may be seen for MCE-S and four peaks for MCM-S and MCH-S in the high-resolution sulfur spectra. The S2p_{3/2} and S2p_{1/2} doublets with binding energies of 164 eV and 165 eV respectively represent the elemental sulfur connected to the oxidation–reduction processes, while the sulfite and sulfone species are related to the small peaks at ~168 eV and >169 eV respectively [52]. From Figure 4D, the amount

of elemental sulfur that is available for redox reactions is largest in the MCE-S material and lowest in the MCH-S material. It is anticipated that this feature will have a significant impact on the electrochemical performance of the battery assembled with MCH-S because it also has the lowest proportion of nitrogen functionalities of the N-pyridinic and N-pyrrolic types which could affect the specific capacity obtained. The MCH-S material, on the other hand, had a larger oxygen content in the bulk, which increased the amount of oxidized sulfur losing active material for redox processes.

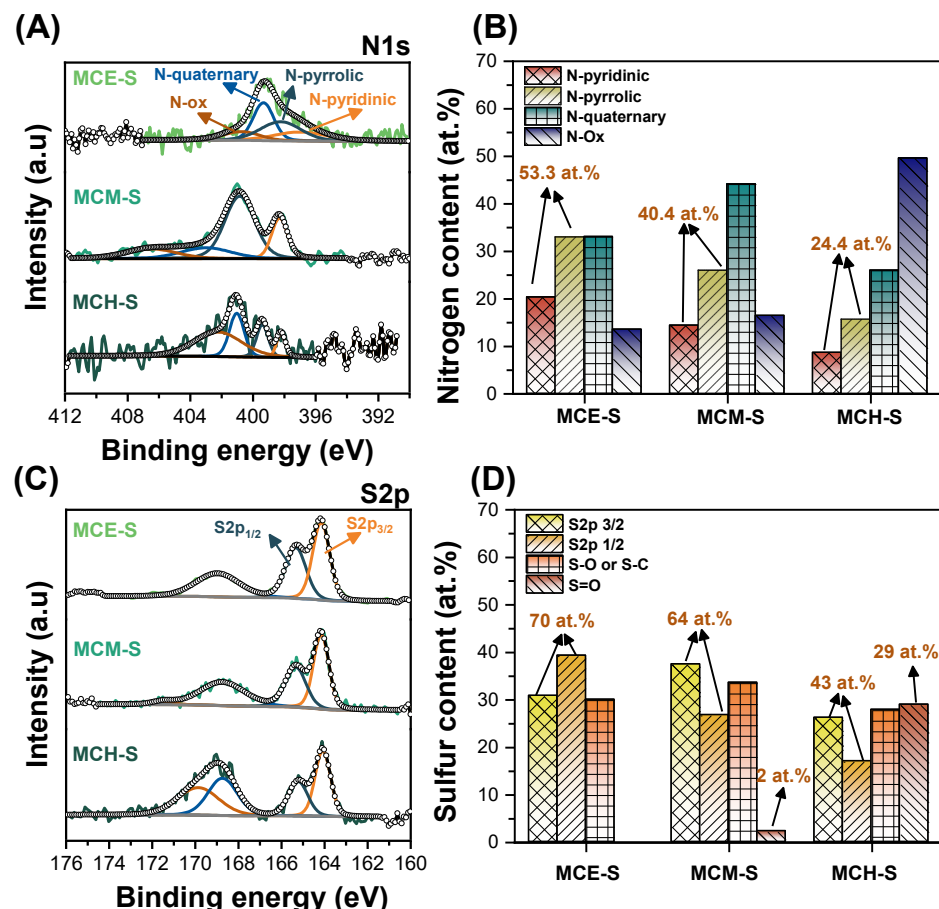


Figure 4. High-resolution XPS spectra for (A) nitrogen N1s with (B) the corresponding nitrogen content and distribution, and (C) high-resolution XPS spectra for sulfur S2p with (D) the corresponding sulfur functionalities.

On the other hand, infrared spectroscopy was used to determine if sulfur was present in the S/C materials formed; the outcomes are shown in Figure S3. It was possible to identify the existence of C-C, C-H, and C=C bonds, which are indicative of carbonaceous structures. The presence of C=O and C-O bonds is due to the materials derived from sucrose leading to the formation of carbonaceous materials with oxygen content. Finally, the inclusion of nitrogen functionalities was evidenced by the presence of C-N and C=N bonds. These results are in agreement with what was observed from XPS [53–55].

3.2. Electrochemical Performance of the Li–S Cells

Figure 5 depicts the electrochemical behavior of the S/C materials when they were used in the assembly of Li–S cells. The Li–S cells' redox process can be seen in the cyclic voltammetry (0.1 mV s^{-1}) presented in Figure 5A, which displays the formation of lithium polysulfide species and their subsequent oxidation to generate elemental sulfur. At 2.4 V and 2.0 V (versus Li^+/Li), respectively, two cathodic peaks are detected for the evaluated cells reflecting the transition of elemental sulfur (S_8) to long-chain lithium polysulfide

species (Li_2S_n , $4 \leq n \leq 8$) and then from long-chain to short-chain yielding insoluble species ($\text{Li}_2\text{S}_2/\text{Li}_2\text{S}$) which agrees with what is reported about the reaction mechanism of these systems [56]. However, only one peak is visible in the anodic scan, which corresponds to the formation of S_8 from its reduced species. The above shows that the materials have strong conductivity, which leads to quick kinetics in a single step. The shape of the voltammogram at low voltages in the cathodic zone is due to the capacitive behavior of the materials since there is a high content of carbonaceous material in the cathodes (~90 wt.%), which means that the shape of the voltammogram tends to retain the behavior of a supercapacitor. The voltage gap (ΔE) between the cathodic peak concerning the initial sulfur reduction step and the anodic peak can be used to determine the reversibility of the processes in each assembled cell; when $\Delta E = 59/n$ mV at 25°C (n = electrons involved in the redox reactions, for Li-S batteries $n = 2$), the process can be considered as reversible and independent of the scan rate. The ΔE was 0.30 V for MCH-S and 0.38 V for MCE-S and MCM-S, respectively, indicating that all cells have low reversibility due to the uncompensated resistance between the sulfur cathode and the lithium anode produced by the formation of insoluble species during the redox reactions affecting the efficiency of the cells; however, the cells evaluated present comparable redox reaction reversibility. According to Figure 5A, an extra cathodic peak (~1.7 V) becomes visible in the evaluation of the three materials. It has been observed that for materials with the presence of micropores such as those evaluated in this work (evidenced in the adsorption/desorption isotherms in which at low relative pressures there is nitrogen adsorption in the micropores, Figure 5A,B), sulfur remains strongly embedded within the micropores, implying that the energy required for the electrochemical process to proceed must be increased rather than favoring the retention of sulfur, resulting in the appearance of new reduction peaks at low potentials. This potential shift may be associated with low-molecular forms of elemental sulfur with a short chain configuration inside micropores, which are unstable due to their high energy state compared to molecules with crown rings [57].

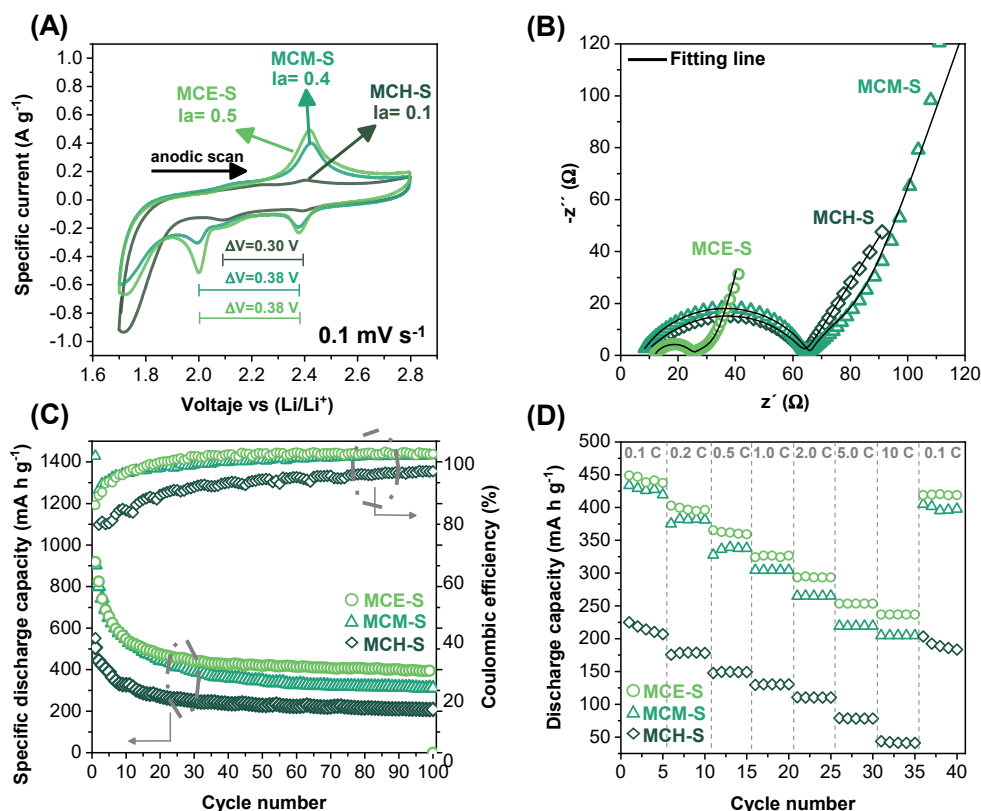


Figure 5. (A) Cyclic voltammetry at 0.1 mV s^{-1} , (B) EIS profiles before cycling, (C) cycling performance at 0.1 C , and (D) C-rate profiles of the materials used in Li-S cells.

The peak current can be used also to determine which cell presents a better electrochemical reversible process, for this, $i_{p,a}/i_{p,c} = 1$; the anodic and cathodic peak ratio was 0.92, 1.23, and 0.89 for MCE-S, MCM-S, and MCH-S, respectively, showing that the cell MCE-S possesses better reversibility with the highest current peaks favoring the electrochemical performance [58].

Electrochemical impedance spectroscopy (EIS) was performed to know the resistance presented by each cell as well as the related diffusion coefficients; Figure 5B presents the Nyquist plot for the studied cells before cycling. A semicircle can be observed related to the resistance to charge transfer (R_{ct}) through the electrode–electrolyte interface which is associated with the efficiency of the oxidation–reduction processes, and at the highest R_{ct} values, there is less charge transfer which leads to a decrease in the charge/discharge capacity of the cell [59]. The electrochemical parameters of the cells obtained by mathematical fitting of the impedances are shown in Table 2, the adjustment was performed using the equivalent circuit shown in Figure S4.

The Nyquist plot is composed of a small semicircle at high frequencies related to the resistance of the electrolyte (R_e) followed by two semicircles produced by the resistance to charge transfer (R_{ct}) and by the dissolution of elemental sulfur and/or formation of short-chain lithium polysulfide species (R_2). The straight line at low frequencies (QD) represents the diffusion process. Here, a constant phase element (CPE) rather than a Warburg element was used to fit the diffusion process [60]. The lowest R_{ct} value is presented by MCE-S; this may be because MCM-S and MCH-S had the largest sulfur content (from Figure S1 c.a 28 wt.% and 40 wt.%, respectively) outside of the pores while MCE-S had the lowest (c.a 23 wt.%), which resulted in a decrease in the contact between the sulfur and the conductive matrix.

Using Equation (1) [61], the diffusion coefficient for each cell can be determined from the data located within the straight line. Where D is the diffusion coefficient, R is the gas constant, T is the absolute temperature, A is the surface area, n is the number of electrons involved in the redox reactions, F is Faraday's constant, C is the ion's concentration, and σ is the Warburg factor obtained from the slope of the relationship between Z' and $w^{-1/2}$.

$$D = \frac{R^2 T^2}{2A^2 n^4 F^4 C^2 \sigma^2} \quad (1)$$

The diffusion coefficient for each of the cells is shown in Table 3. A high diffusivity value indicates that ions are transferred quickly at the cathode/electrolyte interface, facilitating the oxidation–reduction processes. The MCH-S cell has the highest diffusion coefficient ($1.16 \times 10^{-18} \text{ cm}^2 \text{ s}^{-1}$), followed by MCE-S ($9.99 \times 10^{-21} \text{ cm}^2 \text{ s}^{-1}$), and MCM-S ($3.90 \times 10^{-23} \text{ cm}^2 \text{ s}^{-1}$). This characteristic reflects the changes in surface area acquired for carbon materials after introducing sulfur. According to reports, materials with larger specific surface areas have higher ion diffusion rates, resulting in higher charge/discharge capacities [62].

Table 3. Impedance parameters and diffusion coefficients of the cells.

Sample	Before Cycling				
	R_s Ω	R_{ct} Ω	Goodness of Fit	Warburg Factor $\Omega \text{ s}^{-1/2}$	Diffusivity $\text{cm}^2 \text{ s}^{-1}$
MCE-S	11.8	13.3	1.26×10^{-4}	2.989	9.99×10^{-21}
MCM-S	6.90	59.1	1.12×10^{-3}	14.94	3.90×10^{-23}
MCH-S	8.42	56.9	9.44×10^{-4}	0.299	1.16×10^{-18}

The MCH-S material presented the greatest surface area ($681 \text{ m}^2 \text{ g}^{-1}$) followed by the material MCE-S ($676 \text{ m}^2 \text{ g}^{-1}$), and MCM-S ($462 \text{ m}^2 \text{ g}^{-1}$); these results are consistent with the ion diffusion rate provided in Table 3. According to the preceding, this must be related to the charge and discharge capacity of the cells; however, the resistance to charge transfer

caused by the formation of sulfur on the surface of the carbon materials must also be considered. Although the MCH-S cell has the highest diffusion coefficient, it also has a high Rct, which will affect the overall electrochemical performance. MCE-S, on the other hand, has a high diffusion coefficient while also having the lowest resistance to charge transfer. Figure 5C compares the discharge profiles at 0.1 C for the cells studied. The initial discharge capacity was 904 mA h g^{-1} , 919 mA h g^{-1} , and 506 mA h g^{-1} for MCE-S, MCM-S, and MCH-S respectively. During the first 20 cycles, the discharge capacity of the cells decreases significantly. This is due to the formation of short-chain lithium polysulfide species that are deposited on the anode's surface or due to the formation of soluble species in the electrolyte that modify its viscosity, resulting in a decrease in the ion diffusion rate. The nitrogen functionalities developed in the carbon materials become relevant in the reduction of polysulfide species that can migrate toward the anode. According to the specific capacity results presented in Figure 5C, the difference in the nitrogen functionalities of the three materials used led to the MCE-S cell presenting the highest specific discharge capacity. The nitrogen functionality of the N-pyridinic type is mostly related with the retention of lithium polysulfide species; however, a synergistic impact has been found when N-pyrrolic is present [48]. According to the XPS results, the MCE-S material had the highest content of these functionalities. On the other hand, due to the moderate N-quaternary content, the carbon electron conductive characteristics could be preserved. The Coulombic efficiency value slightly higher than 100% is indicative of parasitic processes such as supercapacitor behavior of the cathodes due to the high content of carbonaceous material. Table 4 makes a comparison of studies on carbonaceous materials that contain nitrogen. Most works focus on the development of new materials to host sulfur. However, in this work, the main focus was not on developing new materials to obtain high specific capacity, but the study was focused on understanding the role that nitrogen precursors play in the development of nitrogen functionalities related to the trapping of lithium polysulfides.

Table 4. Comparison of electrochemical characteristics of nitrogen-doped carbonaceous materials.

Carbon Host Materials	S (wt.%)	C-Rate	Initial Capacity (mA h g^{-1})	Capacity Retention (mA h g^{-1})	Cycle #	Contribution	Refs.
N-doped carbon nanosphere from Yolk-double shells	76.0	0.2 C	~900	658	100	Design an electrochemical nanoreactor using a yolk-double shell with highly graphitized outer carbon shell with a gradient of nitrogen content.	[63]
Nitrogen doped reduced Graphene oxide	70.0	0.1 C	~900	1308	200	modification of a commercial polypropylene film (Celgard 2400) by impregnation with the carbonaceous material doped with nitrogen	[64]
Nitrogen-doped porous carbon	60.4	0.2 C	~1280	~900	100	Design of a new nitrogen-doped porous carbon fiber as a host material for Li–S batteries	[65]
MOF-derived nitrogen-doped porous carbon	64.6	0.2 C	1213	1114	100	In-situ growth of small-sized zeolitic imidazolate framework-8 nanoparticles on CNTs	[66]
Nitrogen and phosphorus co-doped hierarchically porous carbon	73.0	1 C	810	575	200	Novel strategy to efficiently trap polysulfides by using nitrogen and phosphorus co-doped hierarchically porous carbon	[65]
Nitrogen-doped mesoporous carbon type CMK3	10	0.1	904	394	100	Evaluation of the effect of the nitrogen precursor on the development of nitrogen functionalities	This work

Figure S5 presents the charge/discharge profiles of the cells at 0.1 C. The cells exhibit two plateaus in the first cycle; one associated with the reduction of sulfur to long-chain species (2.3 V) and the other to short-chain species (2.4 V). This is consistent with the cathodic peak-observed results from CV. Better electrochemical behavior is demonstrated by the longer plateau of the CME-S material-assembled cell, which is correlated with a higher specific capacity. Following multiple cycles of the cells, a decrease in the specific capacity is noted due to an increase in the E_{Δ} between charge and discharge, which is associated with the redox process's lack of reversibility. Nonetheless, the pattern of the CME-S cell having a greater specific capacity and the CMH-S cell having a lower specific capacity persists. The above-mentioned parasitic reactions may be the reason why the discharge capacity is larger than the charge capacity. Moreover, this finding implies that lithium ions may still be taken out of the anode to finish the reduction processes.

Figure 5D shows the behavior of Li-S cells at various discharge rates. From this, a similar trend of specific discharge capacity achieved at 0.1 C can be seen where the Li-S cell using the MCE-S material exhibits the highest value at the various C-rates tested. At high C-rates, the cell using MCH-S material has a much lower specific discharge capacity than the other two cells. This can be attributed to the low content of nitrogen functionalities that are responsible for the retention of lithium polysulfides, resulting in the deactivation of the Li-S cells.

4. Conclusions

Different carbon materials were prepared by varying the nitrogen sources to evaluate the nitrogen functionalities that can be developed from them. The results showed that the use of ethylenediamine favored the formation of N-pyridine and N-pyrrolic type nitrogen in a greater proportion (53.3 at.%) concerning the material obtained from melamine (40.4 at.%), which, having a heterocyclic structure, tends to form a carbon material with a higher proportion of nitrogen in the N-quaternary type. The use of hexadecylamine produced a carbon material with the lowest content of these functionalities (24.4 at.%) which is related to the linear structure with only one terminal amino group, this being the only polymerization site available for the formation of carbon. The material formed from ethylenediamine allowed a greater amount of sulfur to be included within its pores (76.8 wt.% of the total sulfur amount used, i.e., 10 wt. %), making efficient contact between the carbon structure and the active material, favoring the electron conductivity of the sulfur necessary to carry out the oxidation-reduction processes during the charge/discharge of Li-S cells. By using hexadecylamine, it was possible to obtain S/C materials with a greater surface area that favored the diffusion of ions through the material; however, as it had a low nitrogen content and a low proportion of the N-pyridinic and N-pyrrolic functionalities, the specific capacity of these cells decreased significantly through cycling, evidencing the importance of controlling the type of nitrogen functionality in carbon materials to improve the electrochemical performance of Li-S cells. It is concluded that the nitrogen functionality that allows an improvement in the electrochemical performance of the Li-S cells is associated with the N-pyridinic nitrogen that, together with the N-pyrrolic, anchors the lithium polysulfide species that are generated during the operation of the cells more efficiently. Although the electronic conductivity of the materials is a crucial factor for the correct operation of these batteries, it is more relevant to retain the deactivating species in the cathodes to obtain higher specific capacities.

Supplementary Materials: The following supporting information can be downloaded at: <https://www.mdpi.com/article/10.3390/batteries10060169/s1>, Figure S1: Thermal (TGA) behavior of the carbon materials (a) before and (b) after sulfur infiltration. Figure S2: Sulfur amount deposited in carbonaceous materials according to their interaction with them. Figure S3: SEM images and sulfur mapping for MCE-S (left column), MCM-S (center column), and MCH-S (right column). Figure S4: Deconvoluted Raman spectrum for MCM. Figure S5: Equivalent circuit used in the refinement of EIS impedance spectra.

Author Contributions: D.L. and J.L. conceptualized the idea and performed supervision of the work, C.M.S. and J.A. performed the materials, the electrochemical and physicochemical characterization, and worked on writing the original draft. D.L. and J.L. worked in writing, reviewing, and editing. All authors have read and agreed to the published version of the manuscript.

Funding: This research received financial support provided by Universidad de Antioquia UdeA, MinCiencias through the project 890 82079, and Instituto Tecnológico Metropolitano (ITM) for the financial support through project P24101.

Data Availability Statement: Data will be made available on request.

Acknowledgments: The authors acknowledge the financial support provided by Universidad de Antioquia UdeA and Minciencias through the project 890 82079. Jennifer Laverde acknowledges Instituto Tecnológico Metropolitano (ITM) for the financial support through project P24101.

Conflicts of Interest: The authors declare no conflicts of interest.

References

- Wang, C.-Y.; Liu, T.; Yang, X.-G.; Ge, S.; Stanley, N.V.; Rountree, E.S.; Leng, Y.; McCarthy, B.D. Fast Charging of Energy-Dense Lithium-Ion Batteries. *Nature* **2022**, *611*, 485–490. [[CrossRef](#)]
- Beaudin, M.; Zareipour, H.; Schellenberglabe, A.; Rosehart, W. Energy Storage for Mitigating the Variability of Renewable Electricity Sources: An Updated Review. *Energy Sustain. Dev.* **2010**, *14*, 302–314. [[CrossRef](#)]
- Bruce, P.G.; Freunberger, S.A.; Hardwick, L.J.; Tarascon, J.M. Li–O₂ and Li–S Batteries with High Energy Storage. *Nat. Mater.* **2012**, *11*, 19–29. [[CrossRef](#)]
- Liu, W.; Placke, T.; Chau, K.T. Overview of Batteries and Battery Management for Electric Vehicles. *Energy Rep.* **2022**, *8*, 4058–4084. [[CrossRef](#)]
- Chen, Y.; Wang, T.; Tian, H.; Su, D.; Zhang, Q.; Wang, G. Advances in Lithium–Sulfur Batteries: From Academic Research to Commercial Viability. *Adv. Mater.* **2021**, *33*, 2003666. [[CrossRef](#)]
- Barghamadi, M.; Kapoor, A.; Wen, C. A Review on Li–S Batteries as a High Efficiency Rechargeable Lithium Battery. *J. Electrochem. Soc.* **2013**, *160*, A1256–A1263. [[CrossRef](#)]
- Xu, R.; Lu, J.; Amine, K. Progress in Mechanistic Understanding and Characterization Techniques of Li–S Batteries. *Adv. Energy Mater.* **2015**, *5*, 1500408. [[CrossRef](#)]
- Huang, Y.; Lin, L.; Zhang, C.; Liu, L.; Li, Y.; Qiao, Z.; Lin, J.; Wei, Q.; Wang, L.; Xie, Q.; et al. Recent Advances and Strategies toward Polysulfides Shuttle Inhibition for High-Performance Li–S Batteries. *Adv. Sci.* **2022**, *9*, 2106004. [[CrossRef](#)]
- Shi, C.; Takeuchi, S.; Alexander, G.V.; Hamann, T.; O'Neill, J.; Dura, J.A.; Wachsman, E.D. High Sulfur Loading and Capacity Retention in Bilayer Garnet Sulfurized-Polyacrylonitrile/Lithium-Metal Batteries with Gel Polymer Electrolytes. *Adv. Energy Mater.* **2023**, *13*, 2301656. [[CrossRef](#)]
- Ji, X.; Lee, K.T.; Nazar, L.F. A Highly Ordered Nanostructured Carbon-Sulphur Cathode for Lithium-Sulphur Batteries. *Nat. Mater.* **2009**, *8*, 500–506. [[CrossRef](#)]
- Xiao, Q.; Yang, J.; Wang, X.; Deng, Y.; Han, P.; Yuan, N.; Zhang, L.; Feng, M.; Wang, C.; Liu, R. Carbon-Based Flexible Self-Supporting Cathode for Lithium-Sulfur Batteries: Progress and Perspective. *Carbon Energy* **2021**, *3*, 271–302. [[CrossRef](#)]
- Yao, S.; Zhang, C.; He, Y.; Li, Y.; Wang, Y.; Liang, Y.; Shen, X.; Li, T.; Qin, S.; Xiang, J. Functionalization of Nitrogen-Doped Carbon Nanofibers with Polyamidoamine Dendrimer as a Freestanding Electrode with High Sulfur Loading for Lithium-Polysulfides Batteries. *ACS Sustain. Chem. Eng.* **2020**, *8*, 7815–7824. [[CrossRef](#)]
- Wang, T.; He, J.; Cheng, X.-B.; Zhu, J.; Lu, B.; Wu, Y. Strategies toward High-Loading Lithium-Sulfur Batteries. *ACS Energy Lett.* **2023**, *8*, 116–150. [[CrossRef](#)]
- Sun, F.; Wang, J.; Chen, H.; Li, W.; Qiao, W.; Long, D.; Ling, L. High Efficiency Immobilization of Sulfur on Nitrogen-Enriched Mesoporous Carbons for Li–S Batteries. *ACS Appl. Mater. Interfaces* **2013**, *5*, 5630–5638. [[CrossRef](#)]
- Qiu, D.; Zhang, X.; Zheng, D.; Ji, W.; Ding, T.; Qu, H.; Liu, M.; Qu, D. High-Performance Li–S Batteries with a Minimum Shuttle Effect: Disproportionation of Dissolved Polysulfide to Elemental Sulfur Catalyzed by a Bifunctional Carbon Host. *ACS Appl. Mater. Interfaces* **2023**, *15*, 36250–36261. [[CrossRef](#)]
- Zhang, K.; Wang, L.; Cai, W.; Chen, L.-F.; Wang, D.; Chen, Y.; Pan, H.; Wang, L.; Qian, Y. Pyridinic and Pyrrolic Nitrogen-Enriched Carbon as a Polysulfide Blocker for High-Performance Lithium–Sulfur Batteries. *Inorg. Chem. Front.* **2019**, *6*, 955–960. [[CrossRef](#)]
- Yi, G.S.; Sim, E.S.; Chung, Y.-C. Effect of Lithium-Trapping on Nitrogen-Doped Graphene as an Anchoring Material for Lithium–Sulfur Batteries: A Density Functional Theory Study. *Phys. Chem. Chem. Phys.* **2017**, *19*, 28189–28194. [[CrossRef](#)]
- Dong, W.; Wu, Z.; Zhu, X.; Shen, D.; Zhao, M.; Yang, F.; Chang, Q.; Tang, S.; Hong, X.; Dong, Z.; et al. Synergistic Pyridinic N/Pyrrolic N Configurations in RGO/CNT Composite Sulfur Hosts for High-Performance Lithium–Sulfur Batteries. *Chem. Eng. J.* **2024**, *488*, 150872. [[CrossRef](#)]
- Bosubabu, D.; Sampathkumar, R.; Karkera, G.; Ramesha, K. Facile Approach to Prepare Multiple Heteroatom-Doped Carbon Material from Bagasse and Its Applications toward Lithium-Ion and Lithium–Sulfur Batteries. *Energy Fuels* **2021**, *35*, 8286–8294. [[CrossRef](#)]

20. Babu, D.B.; Ramesha, K. Melamine Assisted Liquid Exfoliation Approach for the Synthesis of Nitrogen Doped Graphene-like Carbon Nano Sheets from Bio-Waste Bagasse Material and Its Application towards High Areal Density Li-S Batteries. *Carbon* **2019**, *144*, 582–590. [[CrossRef](#)]
21. Xiang, M.; Yang, L.; Zheng, Y.; Huang, J.; Jing, P.; Wu, H.; Zhang, Y.; Liu, H. A Freestanding and Flexible Nitrogen-Doped Carbon Foam/Sulfur Cathode Composed with Reduced Graphene Oxide for High Sulfur Loading Lithium–Sulfur Batteries. *J. Mater. Chem. A Mater.* **2017**, *5*, 18020–18028. [[CrossRef](#)]
22. Le, H.T.T.; Dang, T.-D.; Chu, N.T.H.; Park, C.-J. Synthesis of Nitrogen-Doped Ordered Mesoporous Carbon with Enhanced Lithium Storage Performance from Natural Kaolin Clay. *Electrochim. Acta* **2020**, *332*, 135399. [[CrossRef](#)]
23. Montiel-Centeno, K.; Barrera, D.; Villarroel-Rocha, J.; Arroyo-Gómez, J.J.; Moreno, M.S.; Sapag, K. CMK-3 Nanostructured Carbon: Effect of Temperature and Time Carbonization on Textural Properties and H₂ Storage. *Chem. Eng. Commun.* **2019**, *206*, 1581–1595. [[CrossRef](#)]
24. Park, H.Y.; Huang, M.; Yoon, T.-H.; Song, K.H. Electrochemical Properties of Kenaf-Based Activated Carbon Monolith for Supercapacitor Electrode Applications. *RSC Adv.* **2021**, *11*, 38515–38522. [[CrossRef](#)]
25. Xu, J.; Dong, G.; Jin, C.; Huang, M.; Guan, L. Sulfur and Nitrogen Co-Doped, Few-Layered Graphene Oxide as a Highly Efficient Electrocatalyst for the Oxygen-Reduction Reaction. *ChemSusChem* **2013**, *6*, 493–499. [[CrossRef](#)]
26. Darwent, B.D. *Bond Dissociation Energies in Simple Molecules*; NSRDS-NBS 31; National Standard Reference Data Series; National Bureau of Standards: Gaithersburg, MD, USA, 1970; 52p.
27. Yang, X.; Li, X.; Adair, K.; Zhang, H.; Sun, X. Structural Design of Lithium–Sulfur Batteries: From Fundamental Research to Practical Application. *Electrochem. Energy Rev.* **2018**, *1*, 239–293. [[CrossRef](#)]
28. Suzuki, K.; Tateishi, M.; Nagao, M.; Imade, Y.; Yokoi, T.; Hirayama, M.; Tatsumi, T.; Kanno, R. Synthesis, Structure, and Electrochemical Properties of a Sulfur-Carbon Replica Composite Electrode for All-Solid-State Li-Sulfur Batteries. *J. Electrochem. Soc.* **2017**, *164*, A6178–A6183. [[CrossRef](#)]
29. Thommes, M. Physisorption of Gases, with Special Reference to the Evaluation of Surface Area and Pore Size Distribution (IUPAC Technical Report). *Chem. Int.* **2016**, *38*, 25. [[CrossRef](#)]
30. Li, X.; Wang, Y.; Xu, C.; Pan, L. Mesoporous Carbon/Sulfur Composite with N-Doping and Tunable Pore Size for High-Performance Li-S Batteries. *J. Solid State Electrochem.* **2017**, *21*, 1101–1109. [[CrossRef](#)]
31. Costa, L.; Camino, G. Thermal Behaviour of Melamine. *J. Therm. Anal.* **1988**, *34*, 423–429. [[CrossRef](#)]
32. Trasobares, S.; Kolczewski, C.; Räty, R.; Borglund, N.; Bassan, A.; Hug, G.; Colliex, C.; Csillag, S.; Pettersson, L.G.M. Monitoring the Decomposition of Melamine in the Solid Phase by Electron Energy Loss Chronospectroscopy. *J. Phys. Chem. A* **2002**, *107*, 228–235. [[CrossRef](#)]
33. Juárez, J.M.; Venosta, L.F.; Anunziata, O.A.; Gómez Costa, M.B. H₂ Storage Using Zr-CMK-3 Developed by a New Synthesis Method. *Int. J. Energy Res.* **2022**, *46*, 2893–2903. [[CrossRef](#)]
34. Sun, Y.; Yu, Y.; Li, D.; Kong, W.; Yang, F. Preparation and Characterization of Carex Meyeriana Kunthcellulose Nanofibers by Electrospinning. *Sci. Rep.* **2022**, *12*, 22207. [[CrossRef](#)]
35. Deng, Z.; Zhang, Z.; Lai, Y.; Liu, J.; Liu, Y.; Li, J. A Sulfur–Carbon Composite for Lithium/Sulfur Battery Based on Activated Vapor-Grown Carbon Fiber. *Solid State Ion.* **2013**, *238*, 44–49. [[CrossRef](#)]
36. Zhao, Z.; Qin, D.; Wang, S.; Chen, G.H.; Li, Z. Fabrication of High Conductive S/C Cathode by Sulfur Infiltration into Hierarchical Porous Carbon/Carbon Fiber Weave-Structured Materials via Vapor-Melting Method. *Electrochim. Acta* **2014**, *127*, 123–131. [[CrossRef](#)]
37. Chen, X.; Guo, R.; Liu, Q.; Yue, W. Improved Lithium Storage Performance of Sulfur Loaded by CMK-3 with a Tailored Hierarchical Pore Structure. *J. Solid State Electrochem.* **2021**, *25*, 2503–2511. [[CrossRef](#)]
38. Olchowski, R.; Zięba, E.; Giannakoudakis, D.A.; Anastopoulos, I.; Dobrowolski, R.; Barczak, M. Tailoring Surface Chemistry of Sugar-Derived Ordered Mesoporous Carbons towards Efficient Removal of Diclofenac from Aquatic Environments. *Materials* **2020**, *13*, 1625. [[CrossRef](#)]
39. Sheng, C. Char Structure Characterised by Raman Spectroscopy and Its Correlations with Combustion Reactivity. *Fuel* **2007**, *86*, 2316–2324. [[CrossRef](#)]
40. Khan, S.; Raj, R.P.; Mohan, T.V.R.; Bhuvaneswari, S.; Varadaraju, U.V.; Selvam, P. Electrochemical Performance of Nano-LiFePO₄ Embedded Ordered Mesoporous Nitrogenous Carbon Composite as Cathode Material for Li-Ion Battery Applications. *J. Electroanal. Chem.* **2019**, *848*, 113242. [[CrossRef](#)]
41. Sadezky, A.; Muckenhuber, H.; Grothe, H.; Niessner, R.; Pöschl, U. Raman Microspectroscopy of Soot and Related Carbonaceous Materials: Spectral Analysis and Structural Information. *Carbon* **2005**, *43*, 1731–1742. [[CrossRef](#)]
42. Claramunt, S.; Varea, A.; López-Díaz, D.; Velázquez, M.M.; Cornet, A.; Cirera, A. The Importance of Interbands on the Interpretation of the Raman Spectrum of Graphene Oxide. *J. Phys. Chem. C* **2015**, *119*, 10123–10129. [[CrossRef](#)]
43. Bokobza, L.; Bruneel, J.-L.; Couzi, M. Raman Spectra of Carbon-Based Materials (from Graphite to Carbon Black) and of Some Silicone Composites. *C* **2015**, *1*, 77–94. [[CrossRef](#)]
44. Hunter, R.D.; Hayward, E.C.; Smales, G.J.; Pauw, B.R.; Kulak, A.; Guan, S.; Schnepf, Z. The Effect of Nitrogen on the Synthesis of Porous Carbons by Iron-Catalyzed Graphitization. *Mater. Adv.* **2023**, *4*, 2070–2077. [[CrossRef](#)]
45. Ugwumadu, C.; Olson, R., III; Smith, N.L.; Nepal, K.; Al-Majali, Y.; Tremblay, J.; Drabold, D.A. Computer Simulation of Carbonization and Graphitization of Coal. *Nanotechnology* **2024**, *35*, 095703. [[CrossRef](#)]

46. Xia, Y.; Wang, C.; Li, R.; Fukuto, M.; Vogt, B.D. Sulfur Diffusion within Nitrogen-Doped Ordered Mesoporous Carbons Determined by in Situ X-Ray Scattering. *Langmuir* **2018**, *34*, 8767–8776. [[CrossRef](#)]
47. Li, B.; Xie, M.; Yi, G.; Zhang, C. Biomass-Derived Activated Carbon/Sulfur Composites as Cathode Electrodes for Li–S Batteries by Reducing the Oxygen Content. *RSC Adv.* **2020**, *10*, 2823–2829. [[CrossRef](#)]
48. Li, L.; Zhou, G.; Yin, L.; Koratkar, N.; Li, F.; Cheng, H.-M. Stabilizing Sulfur Cathodes Using Nitrogen-Doped Graphene as a Chemical Immobilizer for LiS Batteries. *Carbon* **2016**, *108*, 120–126. [[CrossRef](#)]
49. Yamada, Y.; Tanaka, H.; Kubo, S.; Sato, S. Unveiling Bonding States and Roles of Edges in Nitrogen-Doped Graphene Nanoribbon by X-Ray Photoelectron Spectroscopy. *Carbon* **2021**, *185*, 342–367. [[CrossRef](#)]
50. Yin, L.-C.; Liang, J.; Zhou, G.-M.; Li, F.; Saito, R.; Cheng, H.-M. Understanding the Interactions between Lithium Polysulfides and N-Doped Graphene Using Density Functional Theory Calculations. *Nano Energy* **2016**, *25*, 203–210. [[CrossRef](#)]
51. Song, J.; Gordin, M.L.; Xu, T.; Chen, S.; Yu, Z.; Sohn, H.; Lu, J.; Ren, Y.; Duan, Y.; Wang, D. Strong Lithium Polysulfide Chemisorption on Electroactive Sites of Nitrogen-Doped Carbon Composites for High-Performance Lithium-Sulfur Battery Cathodes. *Angew. Chem. Int. Ed.* **2015**, *54*, 4325–4329. [[CrossRef](#)]
52. Li, H.; Li, J.; Xiang, M.; Zhao, Z.; Guo, J.; Yang, Z.; Bai, W.; Yang, X. A Functional Carbon Decorated Separator for the Confinement and Redox Conversion of Lithium Polysulfides in High Sulfur-Loading Lithium Sulfur Batteries. *Electrochim. Acta* **2023**, *469*, 143276. [[CrossRef](#)]
53. Cui, X.; Wang, X.; Pan, Q. Achieving Fast and Stable Li^+ Transport in Lithium-Sulfur Battery via a High Ionic Conduction and High Adhesion Solid Polymer Electrolyte. *Energy Mater.* **2023**, *3*, 300034. [[CrossRef](#)]
54. He, Y.; Shan, Z.; Tan, T.; Chen, Z.; Zhang, Y. Ternary Sulfur/Polyacrylonitrile/SiO₂ Composite Cathodes for High-Performance Sulfur/Lithium Ion Full Batteries. *Polymers* **2018**, *10*, 930. [[CrossRef](#)]
55. Anunciado, M.B.; De Boskey, M.; Haines, L.; Lindskog, K.; Dombek, T.; Takahama, S.; Dillner, A.M. Stability Assessment of Organic Sulfur and Organosulfate Compounds in Filter Samples for Quantification by Fourier-Transform Infrared Spectroscopy. *Atmos. Meas. Tech.* **2023**, *16*, 3515–3529. [[CrossRef](#)]
56. Yu, C.; Jin, Q.; Zhang, L.; Zhao, K.; Zhang, L.; Han, F.; Yao, J.; Lu, H.; Zhang, X.; Wu, L. Synergistic Adsorption-Electrocatalysis of Carbon Nanotubes/Vanadium Sulfide Modified Separator toward High Performance Li–S Batteries. *Electrochim. Acta* **2023**, *438*, 141566. [[CrossRef](#)]
57. Zhang, B.; Qin, X.; Li, G.R.; Gao, X.P. Enhancement of Long Stability of Sulfur Cathode by Encapsulating Sulfur into Micropores of Carbon Spheres. *Energy Environ. Sci.* **2010**, *3*, 1531–1537. [[CrossRef](#)]
58. Huang, X.; Wang, Z.; Knibbe, R.; Luo, B.; Ahad, S.A.; Sun, D.; Wang, L. Cyclic Voltammetry in Lithium–Sulfur Batteries—Challenges and Opportunities. *Energy Technol.* **2019**, *7*, 1801001. [[CrossRef](#)]
59. Zhu, T.; Wu, Q.; Cao, Y.; Wang, W.; Li, Y.; Meng, S.; Liu, L. Study on the Effect of Carbon Nanotubes Loaded with Cobalt Disulfide Modified Multifunctional Separator on Li–S Battery. *Electrochim. Acta* **2023**, *447*, 142145. [[CrossRef](#)]
60. Yan, L.; Gao, X.; Thomas, J.P.; Ngai, J.; Altounian, H.; Leung, K.T.; Meng, Y.; Li, Y. Ionically Cross-Linked PEDOT:PSS as a Multi-Functional Conductive Binder for High-Performance Lithium–Sulfur Batteries. *Sustain. Energy Fuels* **2018**, *2*, 1574–1581. [[CrossRef](#)]
61. Zhu, W.; Xu, W.; Liu, D.; He, L.; Liu, X.; Zhao, Z. Ionic Transport Kinetics of Selective Electrochemical Lithium Extraction from Bines. *Elec. Acta* **2024**, *475*, 143519–143527. [[CrossRef](#)]
62. Qiu, Z.; Cao, F.; Pan, G.; Li, C.; Chen, M.; Zhang, Y.; He, X.; Xia, Y.; Xia, X.; Zhang, W. Carbon Materials for Metal-Ion Batteries. *ChemPhysMater* **2023**, *2*, 267–281. [[CrossRef](#)]
63. Pan, J.; Sun, Y.; Wu, Y.; Li, J.; Huang, W.; Shi, K.; Lin, Y.; Dong, H.; Liu, Q. Yolk-Double Shells Hierarchical N-Doped Carbon Nanosphere as an Electrochemical Nanoreactor for High Performance Lithium-Sulfur Batteries. *Carbon* **2022**, *198*, 80–90. [[CrossRef](#)]
64. Srikaow, A.; Mensing, J.P.; Lohitkarn, J.; Sriprachuabwong, C.; Poochai, C.; Choominjak, Y.; Wisitsoraat, A.; Lomas, T.; Tuantranont, A. Improved Performance of Lithium-Sulfur Batteries Using Nitrogen-Doped Reduced Graphene Oxide-Coated Separators with Optimized Nitrogen Content. *Energy Fuels* **2022**, *36*, 13902–13910. [[CrossRef](#)]
65. Ai, W.; Zhou, W.; Du, Z.; Chen, Y.; Sun, Z.; Wu, C.; Zou, C.; Li, C.; Huang, W.; Yu, T. Nitrogen and Phosphorus Codoped Hierarchically Porous Carbon as an Efficient Sulfur Host for Li–S Batteries. *Energy Storage Mater.* **2017**, *6*, 112–118. [[CrossRef](#)]
66. Chen, J.; Yang, Y.; Yu, S.; Zhang, Y.; Hou, J.; Yu, N.; Fang, B. MOF-Derived Nitrogen-Doped Porous Carbon Polyhedrons/Carbon Nanotubes Nanocomposite for High-Performance Lithium–Sulfur Batteries. *Nanomaterials* **2023**, *13*, 2416. [[CrossRef](#)]

Disclaimer/Publisher’s Note: The statements, opinions and data contained in all publications are solely those of the individual author(s) and contributor(s) and not of MDPI and/or the editor(s). MDPI and/or the editor(s) disclaim responsibility for any injury to people or property resulting from any ideas, methods, instructions or products referred to in the content.